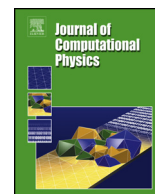# An adaptive finite element method for solving 3D electromagnetic volume integral equation with applications in microwave thermometry

(article starts on next page)

An adaptive finite element method for solving 3D electromagnetic volume integral equation with applications in microwave thermometry

Larisa Beilina [a,*], Morteza Ghaderi Aram [b], Evgenii M. Karchevskii [c]

[a] *Department of Mathematical Sciences, Chalmers University of Technology and University of Gothenburg, SE-42196 Gothenburg, Sweden*
[b] *Department of Electrical Engineering, Chalmers University of Technology, SE-412 96 Gothenburg, Sweden*
[c] *Institute of Computational Mathematics and Information Technologies, Kazan Federal University, 420008 Kazan, Russia*

ABSTRACT

An adaptive finite element method (AFEM) for the numerical solution of an electromagnetic volume integral equation (VIE) is presented. To solve the model VIE, the problem is formulated as an optimal control problem for minimization of Tikhonov's regularization functional. A posteriori error estimates in the obtained finite element reconstruction and in the underlying Tikhonov's functional are derived. Based on these estimates, adaptive finite element algorithms are formulated and numerically tested on the problem of microwave hyperthermia in cancer treatment. In this problem, the temperature change of a target in the computational domain results in the change of its dielectric properties. Numerical examples of monitoring this change show robust and qualitative three dimensional reconstructions of the target using the proposed adaptive algorithms.

1. Introduction

The paper is devoted to the efficient and reliable solution of an electromagnetic volume integral equation (VIE) in three dimensions using an adaptive finite element method (AFEM). Problems of solution of VIE arise in many applications related to biomedical imaging and specially, to the microwave medical imaging. The specific goal of our work is to test several developed algorithms on the problem of monitoring of hyperthermia in order to reconstruct a three-dimensional target in real time.

Different mathematical analytical methods applied for investigation of three-dimensional vector electromagnetic problems related to VIE are presented in [18,19]. Methods applied in computational electromagnetics are widely presented in [20–22], and the recently developed numerical methods for solution of inverse problems in electromagnetics are given in [23–25,33].

An adaptive finite element method for a Fredholm integral equation of the second kind was considered in [1]. In the current work, we consider more complicated case of the VIE since it is an ill-posed problem: the solution of it is sensitive to the small perturbations in the data function and the inverse operator of VIE is not a compact operator, see [7–9]. Thus, the problem of solution of VIE is formulated as an optimal control problem for minimization of Tikhonov's regularization functional.

---

* Corresponding author.
E-mail addresses: larisa@chalmers.se (L. Beilina), ekarchev@yandex.ru (E.M. Karchevskii).

In the paper, we derive a posteriori error estimates in the finite element solution of VIE and in the error of the underlying Tikhonov's functional. To do that, we specify results of [10,29] for the case of electromagnetic volume integral equation and derive new a posteriori error estimates for our specific problem. Another novelty of the current work is that we allow reconstructed function to be discontinuous what leads to new terms with jumps in a posteriori error estimates. We are not aware about some results of application of an adaptive FEM for solution of electromagnetic VIE in three dimensions with application to real-life experiments. We have developed software implemented in Matlab and C++/PETSC for solution of real-life problem of monitoring of hyperthermia which is provided at [38]. Implementation of all algorithms proposed in this work is included in [38].

The main concept of an adaptive finite element method, which we use in this work for solution of VIE, is as follows: since it is not computationally efficient to use very fine mesh during the numerical solution of VIE, an adaptive finite element method allows to obtain good accuracy of the computed solution via local mesh refinements. To be able use this idea, we minimize Tikhonov functional on a sequence of locally refined meshes which are refined based on a posteriori error estimates derived in this work. Finally, different adaptive algorithms are formulated and numerically tested on the real-life problem of monitoring of hyperthermia.

Microwave hyperthermia [11] is used for treatment of cancer and is a good compliment to other types of traditional cancer therapies like radio- and chemo-therapy [12,13]. The main goal of microwave hyperthermia is to increase the tumor temperature to the therapeutic levels of $40 - 44°C$ while keeping healthy tissue at the normal temperature. During this procedure, it is very important to control thermal dose. Thus, there is a need for robust and real-time reconstruction methods which are capable to solve this problem. The problem of microwave hyperthermia is considered as the problem of differential microwave imaging and is formulated in many works, see [14–16]. In the current work, we use similar experimental set-up as in [14–16], and consider an annular phased array system of 16 monopole antennas constructed to work at the ISM band of 915 MHz. This special frequency band is chosen because it provides a good compromise between the penetration depth of the EM waves into biological tissues and the imaging resolution. Moreover, the dielectric changes due to temperature change are significant enough at this frequency band to be detected through microwave imaging techniques. For instance, it is shown in [17] that 1% dielectric change per degree centigrade occurs between $28°C$ and $53°C$ and thus, it can be used in our experiment in the hyperthermic temperature range.

A linear least squares method combined with an adaptive finite element method has been presented in the recent work [5] for solution of microwave hyperthermia thermometry. However, the method considered in the present work is completely different from the AFEM method of [5]: in [5] AFEM was used for solution of image restoration problem in 2D which was formulated as solution of a Fredholm integral equation of the first kind with standard convolution kernel and measurements taken from the solution of least squares problem, see more details in Test 1 of Section 8. Thus, the adaptive method of [5] can be considered as the second method in a two-stage procedure: on the first stage, standard least squares method obtains initial reconstruction of the target, and on the second stage, AFEM improves this reconstruction. AFEM method of [5] has shown significant improvement of reconstruction obtained by the least squares method, via local adaptive mesh refinements. However, VIE was not solved in adaptive algorithm of [5] and thus, real measurements of scattered parameters were not used in it.

In the current work, we fill this gap by solving VIE which describes the process of microwave thermometry in 3D via adaptive algorithms. Our numerical examples of Section 8 show that an adaptive finite element method is a reliable and fast tool to obtain reconstructed images in 3D and thus, this method can be adopted in different microwave applications to obtain real-time feedback.

The paper is outlined as follows. In Section 2, the model VIE is derived from the vector wave equation for the electric field in non-magnetic media, and in Section 3, the mathematical model of VIE is presented. In Section 4, an ill-posed problem is formulated, and Section 5 presents the finite element method for minimization of Tikhonov's functional. Derivation of a posteriori error estimates is developed in Section 6. Section 7 describes different algorithms for solution of our ill-posed problem which are based on a posteriori error estimates of Section 6. Next, 3D numerical examples of reconstruction of the heated object during the process of hyperthermia are presented in Section 8. Finally, we end the work with concluding remarks in section 9.

2. Derivation of the volume integral equation

Let $\Omega \subset \mathbb{R}^3$ be a convex bounded domain with the boundary $\partial\Omega \in C^2$. Following the conventional physical notations of [2], $r = (x, y, z)$ is taken as the position vector in Cartesian coordinates. Our model PDE problem corresponding to volume integral equation is the following vector wave equation (see, for example, [2]) for the electric field $\widehat{E}(r) = (\widehat{E}_1(r), \widehat{E}_2(r), \widehat{E}_3(r))$ in a non-magnetic medium with the Silver-Müller radiation condition at infinity:

$$\nabla \times \nabla \times \widehat{E}(r) - \omega^2 \left(\frac{\varepsilon_r(r)}{c^2} + i\mu_0 \frac{\sigma(r)}{\omega} \right) \widehat{E}(r) = i\omega\mu_0 \widehat{J}(r), \quad r \in \mathbb{R}^3. \tag{1}$$

Here, $\varepsilon_r(r) = \varepsilon(r)/\varepsilon_0$ and $\sigma(r)$ are the relative dielectric permittivity and electric conductivity functions, respectively, ε_0, μ_0 are dielectric permittivity and permeability of free space, respectively, and $c = 1/\sqrt{\varepsilon_0\mu_0}$ is the speed of light in free space. Equation (1) can be obtained by taking the time-dependent Maxwell's equations for the electric field and then representing

in these equations the time-dependent field as $E(r, t) = \widehat{E}(r)e^{-i\omega t}$ and the source function as $J_{source} = \widehat{J}(r)e^{-i\omega t}$, where ω is the angular frequency.

We introduce the spatially distributed complex dielectric function $\varepsilon'(r)$:

$$\varepsilon'(r) = \varepsilon_r(r)\frac{1}{c^2} + i\mu_0\frac{\sigma(r)}{\omega}. \tag{2}$$

Then equation (1) transforms to the vector wave equation

$$\nabla \times \nabla \times \widehat{E}(r) - \omega^2\varepsilon'(r)\widehat{E}(r) = i\omega\mu_0\widehat{J}(r). \tag{3}$$

Subtracting the term $\nabla \times \nabla \times \widehat{E}(r) - \omega^2\varepsilon_b\widehat{E}(r)$ from both sides of (3), we get

$$-\omega^2(\varepsilon'(r) - \varepsilon_b)\widehat{E}(r) = i\omega\mu_0\widehat{J}(r) - \nabla \times \nabla \times \widehat{E}(r) + \omega^2\varepsilon_b\widehat{E}, \tag{4}$$

which can be rewritten as

$$\nabla \times \nabla \times \widehat{E}(r) - \omega^2(\varepsilon'(r) - \varepsilon_b)\widehat{E}(r) = i\omega\mu_0\widehat{J}(r) + \omega^2\varepsilon_b\widehat{E}. \tag{5}$$

Here, ε_b is the dielectric permittivity corresponding to the background medium.

To proceed further, we introduce the dyadic Green's function $\bar{G}(r, r')$ for the problem in a homogeneous medium (see, for example, [2]):

$$\nabla \times \nabla \times \bar{G}(r, r') - \omega^2\varepsilon_b\bar{G}(r, r') = I\delta(r - r'), \quad r \in \mathbb{R}^3, \tag{6}$$

where I is an identity operator. Rewriting equation (5) according to the form of equation (6), we have

$$\nabla \times \nabla \times \widehat{E}(r) - \omega^2\varepsilon_b\widehat{E}(r) = i\omega\mu_0\widehat{J}(r) + \omega^2(\varepsilon'(r) - \varepsilon_b)\widehat{E}(r). \tag{7}$$

We multiply (7) by $\bar{G}(r, r')$ and (6) by $\widehat{E}(r)$, correspondingly, to get:

$$\nabla \times \nabla \times \widehat{E}(r)\bar{G}(r, r') - \omega^2\varepsilon_b\widehat{E}(r)\bar{G}(r, r') = i\omega\mu_0\widehat{J}(r)\bar{G}(r, r') + \omega^2(\varepsilon'(r) - \varepsilon_b)\widehat{E}(r)\bar{G}(r, r'), \tag{8}$$

$$\nabla \times \nabla \times \bar{G}(r, r')\widehat{E}(r) - \omega^2\varepsilon_b\bar{G}(r, r')\widehat{E}(r) = \delta(r - r')\widehat{E}(r). \tag{9}$$

Then subtracting (9) from (8) and integrating, we obtain

$$(\nabla \times \nabla \times \widehat{E}(r), \bar{G}(r, r')) - (\omega^2\varepsilon_b\widehat{E}(r), \bar{G}(r, r')) - (\nabla \times \nabla \times \bar{G}(r, r'), \widehat{E}(r)) + (\omega^2\varepsilon_b\bar{G}(r, r'), \widehat{E}(r))$$
$$= (i\omega\mu_0\widehat{J}(r), \bar{G}(r, r')) + (\omega^2(\varepsilon'(r) - \varepsilon_b)\widehat{E}, \bar{G}(r, r')) - (\delta(r - r'), \widehat{E}(r)). \tag{10}$$

Here, $(\cdot, \cdot)$ denotes the standard scalar product in space.

The above equation is reduced to the following equation

$$(\nabla \times \nabla \times \widehat{E}(r), \bar{G}(r, r')) - (\nabla \times \nabla \times \bar{G}(r, r'), \widehat{E}(r))$$
$$= (i\omega\mu_0\widehat{J}(r), \bar{G}(r, r')) + (\omega^2(\varepsilon'(r) - \varepsilon_b)\widehat{E}, \bar{G}(r, r')) - (\delta(r - r'), \widehat{E}(r)). \tag{11}$$

We use integration by parts for the two terms on the left hand side of (11), see details in [6], and apply the Silver-Müller radiation condition at infinity, to get:

$$(\nabla \times \nabla \times \widehat{E}(r), \bar{G}(r, r')) = (\nabla \times \widehat{E}(r), \nabla \times \bar{G}(r, r')),$$
$$(\nabla \times \nabla \times \bar{G}(r, r'), \widehat{E}(r)) = (\nabla \times \bar{G}(r, r'), \nabla \times \widehat{E}(r)). \tag{12}$$

Applying (12) in the left hand side of (11), we obtain

$$(\nabla \times \nabla \times \widehat{E}(r), \bar{G}(r, r')) - (\nabla \times \nabla \times \bar{G}(r, r'), \widehat{E}(r)) = 0. \tag{13}$$

Using the principle of linear superposition, see details in [2], we finally get from (11) the following equation

$$\widehat{E}(r) = i\omega\mu_0\int_\Omega \widehat{J}(r)\bar{G}(r, r')\,dr + \omega^2\int_\Omega (\varepsilon'(r) - \varepsilon_b)\widehat{E}(r)\bar{G}(r, r')\,dr. \tag{14}$$

The first term in the right hand side of the above equation corresponds to the incident electric field $\widehat{E}_{inc}$, see [2]. Hence, (14) becomes

$$\widehat{E}(r) = \widehat{E}_{inc} + \omega^2\int_\Omega (\varepsilon'(r) - \varepsilon_b)\widehat{E}(r)\bar{G}(r, r')\,dr. \tag{15}$$

According to [4], the scattered field is defined as $\widehat{E}_{sca} = \widehat{E}(r) - \widehat{E}_{inc}$ such that using the reciprocity $\bar{G}(r', r) = \bar{G}(r, r')$ and $O(r) = \varepsilon'(r) - \varepsilon_b(r)$, equation (15) transforms to

$$\widehat{E}_{sca} = \omega^2 \int\limits_{\Omega} \widehat{E}(r) O(r) \bar{G}(r', r) \, dr, \tag{16}$$

which is the model volume integral equation.

3. The mathematical model

The main mathematical model considered in this work is given by the volume integral equation (16) for the scattered field $E_{sca}(r)$ in an inhomogeneous medium which is used in many microwave applications [2–5]. More precisely (see details in the previous section), our mathematical model is given by the volume integral equation in the domain $\Omega \subset \mathbb{R}^3$:

$$\widehat{E}_{sca}(r) = \omega^2 \int\limits_{\Omega} \bar{G}(r', r) O(r) \widehat{E}(r) dr. \tag{17}$$

Here, $\widehat{E}_{sca}(r) = \widehat{E}(r) - \widehat{E}_{inc}(r)$ is the scattered field, $\bar{G}(r', r)$ is the dyadic Green function, $O(r) = \varepsilon'(r) - \varepsilon_b(r)$ is the object function, where $\varepsilon'(r)$ and $\varepsilon_b(r)$ are the complex dielectric permittivity of the medium under investigation and the dielectric permittivity of the background, respectively.

Using the Born approximation $\widehat{E}(r) \approx \widehat{E}_{inc}(r)$ [2] in the right hand side of (17), we obtain the following volume integral equation

$$\widehat{E}_{sca}(r) = \omega^2 \int\limits_{\Omega} \bar{G}(r', r) O(r) \widehat{E}_{inc}(r) dr. \tag{18}$$

According to [4], equation (18) transforms to the following volume integral equation for a bi-static pair of antennas (i, j):

$$S_{j,i}^{sca} = C \int\limits_{\Omega} \widehat{E}_{inc,j}(r) O(r) \widehat{E}_{inc,i}(r) dr, \tag{19}$$

with a constant $C = -\omega^2 \varepsilon_b / 4i\omega\mu$. Using the reciprocity principle in the above equation, $\widehat{E}_{inc,i}$ is the incident electric field produced by the transmitter i and $\widehat{E}_{inc,j}$ is the incident electric field of the receiver j. In the left hand side of (18), the scattered field $\widehat{E}_{sca}(r)$ is replaced with the corresponding scattered S-parameter $S_{j,i}^{scat}$ after introducing the appropriate scaling factor, i.e. C. Therefore, equation (19) uses the scattered S-parameter measurements obtained by a bi-static pair of antennas (i, j) instead of using the scattered electric field $\widehat{E}_{sca}(r)$ and is applied in many microwave applications [2–5] for image reconstruction.

4. Statement of an ill-posed problem

Let W_1, W_2, Q be three Hilbert spaces, $Q \subset W_1$ be a space which is compactly embedded in W_1. We denote scalar products and norms in these spaces, correspondingly, as

$(\cdot, \cdot), \|\cdot\|$ for W_1,

$(\cdot, \cdot)_2, \|\cdot\|_2$ for W_2

and $[\cdot, \cdot], [\cdot]$ for Q.

Let $A : W_1 \rightarrow W_2$ be a bounded linear operator. The volume integral equation (19) can be written in the operator form

$$A(O) = d \tag{20}$$

with an operator $A : W_1 \rightarrow W_2$ defined as

$$A(O) := C \int\limits_{\Omega} \widehat{E}_{inc,j}(r) O(r) \widehat{E}_{inc,i}(r) \, dr \tag{21}$$

and the vector of the right hand side $d = S_{j,i}^{sca}$.

The Problem (P). *Let $O(r) \in W_1$ in*

$$C \int_\Omega \widehat{E}_{inc,j}(r) O(r) \widehat{E}_{inc,i}(r) \, dr = S_{j,i}^{sca}, \tag{22}$$

be unknown in Ω. Determine $O(r)$ for $r \in \Omega$ assuming that $C = -\omega^2 \varepsilon_b / 4i\omega\mu$, $\widehat{E}_{inc,j}(r)$, $\widehat{E}_{inc,i}(r)$ and $S_{j,i}^{sca}$ in (22) are known.

The problem **(P)** of finding a solution to the volume integral equation (22) is an ill-posed problem since it is a Fredholm integral equation of the first kind [9]. To solve the problem **(P)**, we introduce Tikhonov's functional

$$J_\alpha(O) = \frac{1}{2} \|A(O) - d\|_2^2 + \frac{\alpha}{2} [O]^2, \quad d \in W_2, O \in Q, \tag{23}$$

where $\alpha > 0$ is a regularization parameter.

Our goal is to find the function $O \in Q$ which minimizes Tikhonov functional (23). We search for a stationary point of the above functional with respect to O satisfying the following equation for any $b \in Q$:

$$J_\alpha'(O)(b) = 0, \tag{24}$$

where $J_\alpha'(O)$ is the Fréchet derivative of the functional (23).

When the operator A in (20) is such that $A : L_2 \to L_2$, then the following Lemma is valid:

Lemma 1. *Let $A : L_2 \to L_2$ in (20) be a bounded linear operator. Then the Fréchet derivative of the functional (23) is*

$$J_\alpha'(O)(b) = (A^*A(O) - A^*d, b) + \alpha(O, b) \quad \forall b \in Q. \tag{25}$$

For the proof see [9].

When Tikhonov's functional (23) is considered in the form

$$M_\alpha(O) = \frac{1}{2} \|A(O) - d\|_2^2 + \frac{\alpha}{2} \|\nabla O\|^2, \quad d \in W_2, O \in Q, \tag{26}$$

then the following Lemma is valid:

Lemma 2. *Let $A : H^1 \to L_2$ be a bounded linear operator. Then the Fréchet derivative of the functional (26) is*

$$M_\alpha'(O)(b) = (A^*A(O) - A^*d, b) + \alpha(\nabla O, \nabla b) \quad \forall b \in H^1(\Omega), \tag{27}$$

with a convex growth factor b, i.e., $|\nabla b| < b$. The proof follows from Lemma 2 in [26].

The next Lemma is known for a bounded linear operator. We formulate this lemma for our specific case of the functional (23).

Lemma 3. *Let the operator $A : W_1 \to W_2$ be a bounded linear operator which has the Fréchet derivative of the functional (23). Then the functional $J_\alpha(O)$ is strongly convex on the space Q and*

$$\left(J_\alpha'(O_1) - J_\alpha'(O_2), O_1 - O_2\right) \ge \gamma [O_1 - O_2]^2 \quad \forall O_1, O_2 \in Q. $$

5. The finite element method for minimization of Tikhonov functional

We discretize the computational domain $\Omega \subset \mathbb{R}^3$ into elements K satisfying the minimal angle condition [27,28] by the mesh $K_h = \{K\}$. Let $h = h(r)$ be the mesh function such that

$$h|_K = h_K \quad \forall K \in K_h, \tag{28}$$

where h_K is the diameter of K which we define as the longest side of K.

We define the finite element space $V_h \subset V$ as

$$V_h = \left\{ v \in L_2(\Omega) : v \in C(\Omega), \ v|_K \in P_1(K) \ \forall K \in K_h \right\}, \tag{29}$$

where $P_1(K)$ denotes the set of piecewise-linear functions on K.

Let us formulate the finite element method (FEM) for the functional (26). The FEM for the functional (23) with $A : L_2 \to L_2$ can be formulated in a similar fashion with only one distinction in the formulation of the regularization term.

To find optimal solution O of the functional (26), the following problem should be solved:

$$M'(O)(v) = (A^*(A(O) - d), v) + \alpha(\nabla O, \nabla v) = 0. \tag{30}$$

The finite element method for (30) reads: find $O_h \in V_h$ such that for all $v \in V_h$

$$M'(O_h)(v) = (A^*(A(O_h) - d), v) + \alpha(\nabla O_h, \nabla v) = 0. \tag{31}$$

The function O is approximated by $O_h \in V_h$, such that

$$O_h = \sum_{i=1}^{N} O_i \varphi_i, \tag{32}$$

where $\{\varphi_i\}_{i=1}^{N}$ are the standard continuous piecewise linear functions and O_i denote the unknown discrete function-values at the mesh point $r_i \in K_h$.

Substituting (32) into (31) with $v = \varphi_j$, we get the discrete system of equations

$$\sum_{i,j=1}^{N} (A\varphi_i, A\varphi_j)O_i - \sum_{i,j=1}^{N} (d_{h_i}, A\varphi_j) + \alpha \sum_{i,j=1}^{N} (\nabla\varphi_i, \nabla\varphi_j)O_i = 0. \tag{33}$$

This system can be rewritten as

$$\sum_{i,j=1}^{N} (A\varphi_i, A\varphi_j)O_i + \alpha \sum_{i,j=1}^{N} (\nabla\varphi_i, \nabla\varphi_j)O_i = \sum_{i,j=1}^{N} (d_{h_i}, A\varphi_j), \tag{34}$$

which is equivalent to the following linear system of equations

$$(\mathbf{A} + \alpha\mathbf{K})\mathbf{O} = \mathbf{d}. \tag{35}$$

In system (35), matrices $\mathbf{A}$, $\mathbf{K}$ are the finally assembled block matrices, corresponding to the first two terms in the left hand side of (34). $\mathbf{O}$ denotes the vector of nodal values of finite element approximation O_h, and $\mathbf{d}$ is the finally assembled right hand side of (34). In (33), d_h is the nodal interpolant of d.

From (33), we also get the discrete gradient which will be used in the iterative update of algorithms in Section 7:

$$M'(O_h)(\varphi_j) = \sum_{i,j=1}^{N} (A\varphi_i, A\varphi_j)O_i - \sum_{i,j=1}^{N} (d_{h_i}, A\varphi_j) + \alpha \sum_{i,j=1}^{N} (\nabla\varphi_i, \nabla\varphi_j)O_i. \tag{36}$$

6. A posteriori error estimates

In this section, we outline main derivations of a posteriori error estimates for the following errors:

- for the error $\|J_\alpha(O) - J_\alpha(O_h)\|$ in Tikhonov functional (23);
- for the errors $\|O - O_h\|$ in the computed solution O_h.

To make it clear how a posteriori error for the error in Tikhonov functional (23) can be obtained, we present general framework for it, see details in [29].

First we note that

$$J_\alpha(O) - J_\alpha(O_h) = J'_\alpha(O_h)(O - O_h) + R(O_h), \tag{37}$$

where $R(O_h) = O(\|O - O_h\|^2)$ is the remainder of the second order. We assume that the computed finite element approximation O_h of O is close to the regularized solution O of (23). Thus, the term $R(O_h) \rightarrow 0$ and we can neglect it in (37).

Let P_h be the $L_2(\Omega)$ orthogonal projection operator. We define by f_h^I the standard nodal interpolant [30] of f into the space of continuous piecewise-linear functions on the mesh K_h. Then by one of properties of the orthogonal projection, we have

$$\|f - P_h f\|_{L_2(\Omega)} \le \left\| f - f_h^I \right\|_{L_2(\Omega)}. \tag{38}$$

It follows from [32] that

$$\|f - P_h f\|_{L_2(\Omega)} \le C_I h \| f \|_{H^1(\Omega)} \quad \forall f \in H^1(\Omega), \tag{39}$$

where $C_I = C_I(\Omega)$ is a positive constant depending only on the domain Ω.

We now use the splitting

$$O - O_h = (O - O_h^I) + (O_h^I - O_h), \tag{40}$$

together with the Galerkin orthogonality principle

$$J'_\alpha(O_h)(b) = 0 \ \ \forall b \in V_h. \tag{41}$$

Now by inserting (40) into (37), we get the following error representation:

$$J_\alpha(O) - J_\alpha(O_h) \approx J'_\alpha(O_h)(O - O_h^I). \tag{42}$$

In (40) and (42) functions $O_h^I \in V_h$ denote the interpolants of O.

To derive the error $\|O - O_h\|$ in the reconstructed function O_h, we will use the convexity property of Tikhonov functional (23) with the convexity parameter γ

$$\gamma \|O_1 - O_2\|^2 \leq \left\|(J'_\alpha(O_1) - J'_\alpha(O_2), O_1 - O_2)\right\| \ \ \forall O_1, O_2 \in H_1, \tag{43}$$

together with the interpolation property (39).

In the proofs of Theorems 1 and 2, we allow the function O to be discontinuous along the faces of elements K in K_h and introduce notion of jump. We denote the jump of the function O_h computed from the two neighboring elements K^+ and K^- sharing the common side as

$$[O_h] = O_h^+ - O_h^-. \tag{44}$$

We now make both error estimates more explicit.

6.1. A posteriori error estimate in the computed solution

In this section, we derive a posteriori error estimate for the error $\|O - O_h\|$ in the computed solution O_h of the functional (23). Let the scalar product be given by $(\cdot, \cdot)_{L_2} := (\cdot, \cdot)$, as well as norms $\|\cdot, \cdot\|_{L_2} := \|\cdot, \cdot\|$. Whenever the norm should be specified, we will write it henceforth. We denote by

$$V_1(O) = \left\{ O' \in H_1 : \left\| O' - O \right\| < 1 \ \ \forall O \in H_1 \right\}. \tag{45}$$

Theorem 1. *Let $O_h \in V_h$ be a finite element approximations of the regularized solution $O \in H^1(\Omega)$ on the finite element mesh K_h and O^* be the exact solution of* (20). *Then there exists a constant $D = Const. > 0$ satisfying Lipschitz continuity property*

$$\left\| J'_\alpha(O_1) - J'_\alpha(O_2) \right\| \leq D \left\| O_1 - O_2 \right\| \ \ \forall O_1, O_2 \in V_1(O^*) \tag{46}$$

in a small neighborhood of the exact solution O^*, such that the following a posteriori error estimate holds

$$\|O - O_h\| \leq \frac{D}{\gamma} C_I (\|hO_h\| + \|[O_h]\|) \ \ \forall O_h \in V_h. \tag{47}$$

Here, the constant D can be chosen as $D = \|J''_\alpha(O_h)\|$.

Proof. Let O_h be a finite element approximation of O and be the minimizer of Tikhonov functional (23). According to Lemma 3, the functional (23) is strongly convex on the space L_2 with the strong convexity constant γ. This implies, see (43), that

$$\gamma \|O - O_h\|^2_{L_2(\Omega)} \leq \| \left(J'_\alpha(O) - J'(O_h), O - O_h \right) \|_{L_2(\Omega)}, \tag{48}$$

where $J'_\alpha(O_h), J'_\alpha(O)$ are the Fréchet derivatives of the functional (23).

Next, we use the splitting

$$O - O_h = \left(O - O_h^I \right) + \left(O_h^I - O_h \right)$$

and substitute it in (48) to obtain

$$\gamma \|O - O_h\|^2_{L_2(\Omega)} \leq \| \left(J'_\alpha(O) - J'(O_h), O - O_h^I \right) \|_{L_2(\Omega)} + \| \left(J'_\alpha(O) - J'(O_h), O_h^I - O_h \right) \|_{L_2(\Omega)}. \tag{49}$$

Here, O_h^I is the standard interpolant of O.

Applying the Galerkin orthogonality principle (noting that $J'_\alpha(O) = 0$)

$$\left(J'_\alpha(O_h) - J'_\alpha(O), O^I_h - O_h\right) = 0 \tag{50}$$

in (49), we will get

$$\gamma \|O - O_h\|^2_{L_2} \leq \|(J'_\alpha(O) - J'_\alpha(O_h), O - O^I_h)\|_{L_2(\Omega)}. \tag{51}$$

The right hand side of (51) can be estimated using (46) as

$$\| \left(J'_\alpha(O) - J'_\alpha(O_h), O - O^I_h\right) \| \leq D \|O - O_h\| \cdot \|O - O^I_h\|.$$

Substituting the above equation into (51), we obtain

$$\|O - O_h\| \leq \frac{D}{\gamma} \|O - O^I_h\|. \tag{52}$$

Using the interpolation property

$$||O - O^I_h||_{L^2(\Omega)} \leq C_I ||h\, O||_{H^1(\Omega)},$$

we obtain a posteriori error estimate with the interpolation constant C_I:

$$\|O - O_h\| \leq \frac{D}{\gamma} \|O - O^I_h\| \leq \frac{D}{\gamma} C_I \|h\, O\|_{H^1(\Omega)}. \tag{53}$$

We can estimate $\|h\, O\|_{H^1(\Omega)}$ as

$$\begin{aligned}
\|h\, O\|_{H^1(\Omega)} &\leq \sum_K ||h_K O||_{H^1(K)} = \sum_K ||(O + \nabla O) h_K||_{L_2(K)} \\
&\leq \sum_K \left(||O_h h_K||_{L_2(K)} + \left\| \frac{[O_h]}{h_K} h_K \right\|_{L_2(K)}\right) \\
&\leq \|h O_h\|_{L_2(\Omega)} + \|[O_h]\|.
\end{aligned} \tag{54}$$

In (54), $[O_h]$ is the jump of the function O_h over the element K defined as in (44), h_K is the diameter of the element K. In (54) we applied the estimate

$$|\nabla O| \leq \frac{|[O_h]|}{h_K},$$

which is used often in finite element analysis, see for example, [31].

Substituting the above estimates into the right hand side of (53), we get

$$\|O - O_h\| \leq \frac{D}{\gamma} C_I \|h O_h\| + \frac{D}{\gamma} C_I \|[O_h]\| \quad \forall O_h \in V_h.$$

The constant D can be estimated as follows. First we note that by the definition of the Frechét derivative of Tikhonov functional (23) we can write $\forall O_1, O_h \in V_1(O^*)$:

$$J'_\alpha(O_1) - J'_\alpha(O_h) = J''_\alpha(O_h)(O_1 - O_h) + R(O_1, O_h), \tag{55}$$

where the remainder $R(O_1, O_h) = O(\|O_1 - O_h\|^2)$, $(O_1 - O_h) \to 0$ $\forall O_1, O_h \in V_h$, is small and can be neglected. Then

$$\|J'_\alpha(O_1) - J'_\alpha(O_h)\| \leq \|J''_\alpha(O_h)\| \cdot \|O_1 - O_h\|. \tag{56}$$

Comparing (56) with (46), we conclude that $D = \|J''_\alpha(O_h)\|$. □

6.2. A posteriori error estimates for Tikhonov functional

In Theorem 2, we derive a posteriori error estimates for the error in Tikhonov functional (23) obtained on the finite element mesh K_h.

Theorem 2. *Suppose that there exists a minimizer $O \in H^1(\Omega)$ of Tikhonov functional (23) on the mesh K_h. Suppose also that there exists a finite element approximation O_h of O for $J_\alpha(O)$ on the mesh K_h with the mesh function h. Then the following approximate a posteriori error estimate for the error $e = ||J_\alpha(O) - J_\alpha(O_h)||$ in Tikhonov functional (23) holds:*

$$e = ||J_\alpha(O) - J_\alpha(O_h)|| \leq C_I \left\|J'_\alpha(O_h)\right\| (\|h O_h\| + \|[O_h]\|). \tag{57}$$

Proof. By the definition of the Frechét derivative of Tikhonov functional (23) with O and approximation O_h, we have

$$J_\alpha(O) - J_\alpha(O_h) = J'_\alpha(O_h)(O - O_h) + R(O, O_h), \tag{58}$$

where the remainder $R(O, O_h) = O(\|O - O_h\|^2)$, $(O - O_h) \to 0$ for all $O, O_h \in V_h$. Thus, we can neglect the term $R(O, O_h)$ in the estimate (58). We again use the splitting (49) and the Galerkin orthogonality [30]

$$J'_\alpha(O_h)(O_h^I - O_h) = 0 \quad \forall O_h^I, O_h \in V_h \tag{59}$$

to get

$$J_\alpha(O) - J_\alpha(O_h) \le J'_\alpha(O_h)(O - O_h^I), \tag{60}$$

where O_h^I is a standard interpolant of O on the mesh K_h [30].

Taking norms in (60), we get

$$\|J_\alpha(O) - J_\alpha(O_h)\| \le \|J'(O_h)\| \|O - O_h^I\|, \tag{61}$$

where the term $\|O - O_h^I\|$ can be estimated through the following interpolation estimate

$$\|O - O_h^I\|_{L_2(\Omega)} \le C_I \|h\, O\|_{H^1(\Omega)}.$$

Substituting above estimate into (61), we get

$$\|J_\alpha(O) - J_\alpha(O_h)\| \le C_I \left\| J'_\alpha(O_h) \right\| \|h\, O\|_{H^1\Omega)}. \tag{62}$$

We can estimate $\|h\, O\|_{H^1(\Omega)}$ in the right hand side of (62) similar to (54) to get the final estimate as follows

$$\|J_\alpha(O) - J_\alpha(O_h)\| \le C_I \left\| J'_\alpha(O_h) \right\| (\|hO_h\| + \|[O_h]\|) \ \forall O_h \in V_h. \tag{63}$$

Here, $J'_\alpha(O_h)$ is the Frechet derivative given by (64) for $A : H^1 \to L_2$. For $A : L_2 \to L_2$ the Frechet derivative is derived in a similar fashion as in Section 5 and will be

$$J'(O_h)(\varphi_j) = \sum_{i,j=1}^{N} (A\varphi_i, A\varphi_j)O_i - \sum_{i,j=1}^{N} (d_{hi}, A\varphi_j) + \alpha \sum_{i,j=1}^{N} (\varphi_i, \varphi_j)O_i. \quad \square \tag{64}$$

7. Algorithms for solution of the ill-posed problem

In this section, we formulate different algorithms for the solution of the ill-posed problem (**P**): conventional conjugate gradient algorithm (CG) and two different versions of adaptive finite element algorithms, AFEM2 and AFEM3.

The conjugate gradient Algorithm 1 (CG) can be used on the coarse as well as on the l times refined finite element mesh $K_l := K_{hl}$. Let $O_l := O_{hl}$ is the finite element reconstruction obtained on l times refined mesh K_l. The adaptive Algorithm 2 (AFEM2) is based on the solution of linear system of equation (35) obtained after finite element discretization of the functional (26) for $A : H^1 \to L_2$, or the functional (23) for $A : L_2 \to L_2$, to get the reconstruction O_l on l times refined mesh K_l. The Adaptive Algorithm 3 (AFEM3) first uses the discrete gradient g_l on the l times adaptively refined mesh K_l and then the conjugate gradient method (Algorithm 1) to update the reconstruction O_l.

7.1. Conjugate gradient algorithm

In this algorithm, we denote the gradient for $A : H^1 \to L_2$ for the functional (26) by

$$g^n := g^n(r) = (A(O_h^n) - d_h)Av + \alpha \nabla O_h^n \nabla v, \tag{65}$$

where n is the number of iteration in the conjugate gradient Algorithm 1 and function O_h^n is the computed finite element solution of (31) at the iteration n of this algorithm.

Similarly, we denote the gradient of the functional (23) for $A : L_2 \to L_2$ by

$$g^n := g^n(r) = (A(O_h^n) - d_h)Av + \alpha O_h^n v. \tag{66}$$

Algorithm 1 Conjugate Gradient algorithm (CG).

1: Discretize the computational space domain Ω using the finite element mesh K_h. Choose the regularization parameter α. Start with the initial approximations $O_h^0 = O_0$ and compute the sequences of O_h^n in the following steps:

2: Compute gradient g^n via (65) for $A : H^1 \to L_2$ or via (66) for $A : L_2 \to L_2$.

3: Update the function $O_h := O_h^{n+1}$ on K_h via the conjugate gradient method

$$O_h^{n+1} = O_h^n + \psi d^n,$$

where

$$d^n = -g^n + \beta_O^n d^{n-1}$$

with

$$\beta_O^n = \frac{\|g^n\|^2}{\|g^{n-1}\|^2}.$$

Here, $d^0 = -g^0$, and ψ is the step-sizes in the gradient update.

4: For the chosen tolerance θ, stop computing O_h^n at the iteration $M := n$ and obtain the function $O_h^M := O_h^n$ if either $\|g^n\|_{L_2(\Omega)} \le \theta$ or norms $\|O_h^n\|_{L_2(\Omega)}$ are stabilized. Otherwise set $n := n + 1$ and go to step 2.

7.2. Adaptive algorithms

In this section, we present two different adaptive algorithms for the solution of our ill-posed problem (**P**). The adaptive Algorithm 1 is based on solution of the system of linear equations (SLE) (35) while the adaptive Algorithm 2 uses computation of the discrete gradient (65) for the functional (26) when $A : H^1 \to L_2$, or the discrete gradient (66) for the functional (23) in the case when $A : L_2 \to L_2$.

Both algorithms refine the finite element mesh locally using a posteriori error estimates provided by Theorems 1 and 2. These estimates allow us to improve the accuracy of the reconstruction O_h of the problem **P**. First, using the estimate (47) in Theorem 1, we can conclude that the maximum of the computed error $|O - O_h|$ in the reconstructed function O_h is located in neighborhoods of such points in the finite element mesh K_h where the computed $|hO_h| + |[O_h]|$ achieves its maximal value. Next, the estimate (57) of Theorem 2 tells us that the maximum of the error in Tikhonov's functional $|J_\alpha(O) - J_\alpha(O_h)|$ is bounded by the residual $|J'_\alpha(O_h)|$ multiplied by weights $|hO_h\| + |[O_h]|$ and is located in the neighborhoods of mesh points where the product of the residual by weights attains its maximal value.

Thus, the idea of the local finite element mesh refinement of both adaptive algorithms is that it should be refined all neighborhoods of all points in the mesh K_h where the computed $|hO_h| + |[O_h]|$ achieves its maximum values or where $|J'_\alpha(O_h)|$ achieves its maximal values.

We define the minimizer of Tikhonov functional (23) as O, its approximated finite element solution O_h^l on l times adaptively refined mesh $K_l := K_{h_l}$ as O_l and gradient computed on the mesh K_l as g_l. Let us define by $O_M := O_h^M$ and $g_M := g_h^M$ values of approximated function and computed gradient, respectively, obtained after M iterations of the conjugate gradient algorithm.

Algorithm 2 Adaptive algorithm using solution of SLE (AFEM2).

1: Generate the initial FEM mesh K_0 in Ω. Compute the sequence of reconstructions O_l, $l \ge 0$, on the refined meshes, in the following steps:

2: Determine the optimal regularization parameter α_l. Compute the finite element solution O_l on K_l by solving the system of linear equations (35).

3: Use Theorems 1 and 2 for refinement: refine locally the mesh K_l at all points where

$$|R(O_l)| \ge \beta_1 \max_\Omega |R(O_l)|, \tag{67}$$

or where

$$|g_l| \ge \beta_2 \max_\Omega |g_l|. \tag{68}$$

Here, $R(O_l) = |hO_l| + |[O_h]|$, g_l is computed as in (65) and $\beta_{1,2} \in (0, 1)$ should be chosen computationally, see Remark 1.

4: Construct a new mesh K_{l+1} in Ω. Interpolate d_l to d_{l+1} and O_l to O_{l+1}.

5: For the chosen tolerance θ, stop computing O_l at the iteration $M := l$ and obtain the function O_M if either $\|g_l\|_{L_2(\Omega)} \le \theta$ or norms $\|O_l\|_{L_2(\Omega)}$ are stabilized. Otherwise go to step 2.

Remark 1. In adaptive Algorithms 2 and 3, the number of elements in the refined mesh is controlled by the parameters $\beta_{1,2} \in (0, 1)$. The values of these parameters depend on the values of computed $\max_\Omega |R(O_l)|$ and $\max_\Omega |g_l|$ at Step 3 of both algorithms. The computational mesh K_l will be refined in very narrow region if values of $\beta_{1,2}$ will be chosen close to 1. And opposite, if we will choose $\beta_{1,2}$ close to 0, then almost all elements in the finite element mesh K_l will be refined. Numerical tests of Section 8 show that values $\beta_{1,2} \in [0.3, 0.5]$ are optimal one since these values provide refinement exactly at such places of K_l where the inclusion is located.


Algorithm 3 Adaptive algorithm using conjugate gradient algorithm (AFEM3).

1: Generate the initial FEM mesh K_0 in Ω. Compute the sequence of reconstructions O_l, $l \geq 0$, on the refined meshes, in the following steps:

2: Determine the optimal regularization parameter α_l. Compute the gradient g_l as in (65) and then the finite element solution O_l on K_l as in the conjugate gradient Algorithm 1.

3: Refine locally the mesh K_l as at the step 3 of Algorithm 2.

4: Construct a new mesh K_{l+1} in Ω. Interpolate d_l to d_{l+1} and O_l to O_{l+1}.

5: For the chosen tolerance θ, stop computing O_l at the iteration $M := l$ and obtain the function O_M if either $\|g_l\|_{L_2(\Omega)} \leq \theta$ or norms $\|O_l\|_{L_2(\Omega)}$ are stabilized. Otherwise go to step 2.

$$\min_O J_\alpha(O) = \frac{1}{2}\|A(O) - d\|_2^2 + \frac{\alpha}{2}\|O\|^2$$
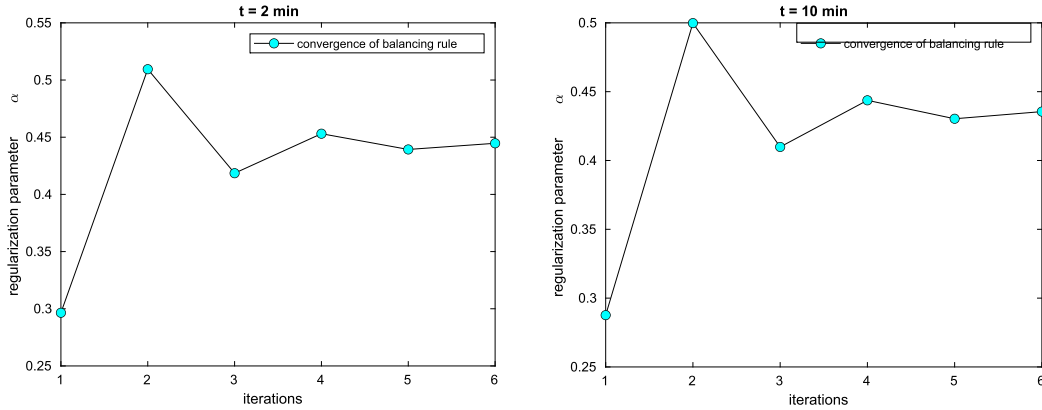
$$\min_O J_\alpha(O) = \frac{1}{2}\|A(O) - d\|_2^2 + \frac{\alpha}{2}\|\nabla O\|^2$$
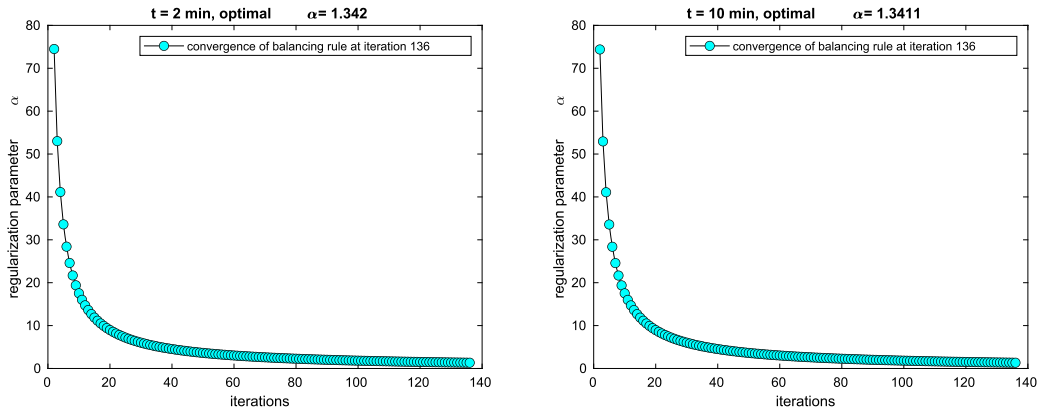

Fig. 1. Test 1. Convergence of fixed point algorithm for computation of the optimal regularization parameter α using balancing principle for the functional (23): top row is for the operator $A : L_2 \to L_2$, bottom row is for the operator $A : H^1 \to L_2$. Tests are done for the conjugate gradient Algorithm 1 without adaptive mesh refinement.

Remark 2. In some computations of Section 8 which results are reported in Tests 1, 2 and Table 2, the Balancing principle [34] was used at step 2 of adaptive Algorithms 2 and 3, for optimal computation of the regularization parameter α. The balancing principle was implemented via fixed point algorithm of [5]. Different algorithms can be chosen for optimal computation of regularization parameter α, see [9,34] and references therein for details of these algorithms.

8. Numerical results

In this section, we present numerical results for solution of the ill-posed problem (**P**) using all algorithms of Section 7 as well as the adaptive finite element algorithm (AFEM1) of [5]. The goal of our simulations is to demonstrate performance
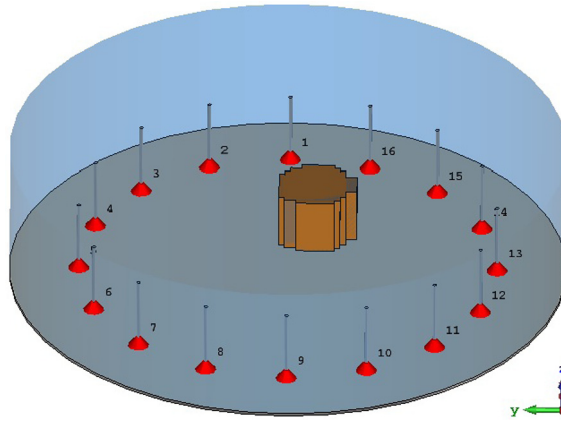
Fig. 2. Simulation setup of CST showing the irregular target, imaging tank, and 16 monopole antennas.

Table 1
The cooling process of a target is simulated where its temperature changes from 55 °C to 29 °C over a ten-minute window of time. As a result of this temperature change, there are changes in permittivity and conductivity of the target.

Timeline (min)	$t = 0$ (Baseline)	$t = 2$	$t = 4$	$t = 6$	$t = 8$	$t = 10$
$\varepsilon_r(t)$	26	28	29	29.8	30.5	31
$\sigma_r(t)$ (S/m)	0.12	0.15	0.19	0.21	0.23	0.24
Coupling fluid 20:7 isopropyl : water ($\varepsilon_r = 24.5$, $\sigma = 0.46$)						

of all algorithms to reconstruct the function O in terms of location/shape and computational time. All simulations were performed in linux on Intel(R) Core(TM) i7-9700 CPU @ 3.00 GHz computer with the software package WavES [37]. The software and perl scripts are provided at [38].

For the full-wave EM simulation, CST Microwave Studio [35] was used to simulate the scenario as shown in Fig. 2. We use the same antenna set-up for all experiments as in [5]. Let us briefly present it now. All of the 16 monopole antennas, optimized to work at 915 MHz, are immersed in a coupling fluid which is a 20:7 alcohol:water mixture as suggested in [15]. The choice of the matching liquid is based on a trade-off to achieve a balance between conductive loss, relative permittivity, and antenna matching.

An off-centered cylindrical inclusion with an irregular cross-section in the x-y plane is considered as the target, and its initial state at $t = 0$ is labeled as the baseline. The dielectric parameters of the target were then changed in a parametric sweep of CST according to Table 1 to imitate the dynamic process of the cooling over a 10-minute window of time. These changes in dielectric properties due to the temperature change are the extrapolated version of those reported in [15]. Finally, the obtained S-parameter at each time step is subtracted from that of the baseline to feed the reconstruction algorithms with a differential input.

Compared with 2D finite element reconstructions of [5], here we show performance of all adaptive algorithms in 3D. The dimensionless computational domain is set as

$$\Omega = \{(x, y, z) : x \in [0, 39], y \in [0, 41], z \in [0, 25]\}$$

and the mesh size h was $h = 0.002$ in x, y and z directions. The optimal value of the regularization parameter α in all methods was computed via balancing principle by the fixed point algorithm of [5] for an initial guess of the regularization parameter $\alpha_0 = 1.0$.

All computations were performed on a workstation with one processor. However, since it uses C++/PETSc [36], then in principle, it can be executed on many processors as PETSc supports parallel implementations. We have estimated the computational time using the following formula for relative time T_r

$$T_r = \frac{t}{(l+1)n}. \tag{69}$$

Here, t is the total computational time, n is the total number of nodes in all refined meshes, and $l = 0, 1, \ldots$ is the number of mesh refinements.

Performance comparison of different reconstruction algorithms was computed and computational times (in seconds) are presented in Table 2 while Table 3 presents the relative computational time of the AFEM-based methods. The tolerance in the stopping criterion in all algorithms was $\theta = 5e{-}15$. Fig. 3 also shows that an adaptive finite element method improves the reconstruction obtained by the least squares method via local adaptive mesh refinements.
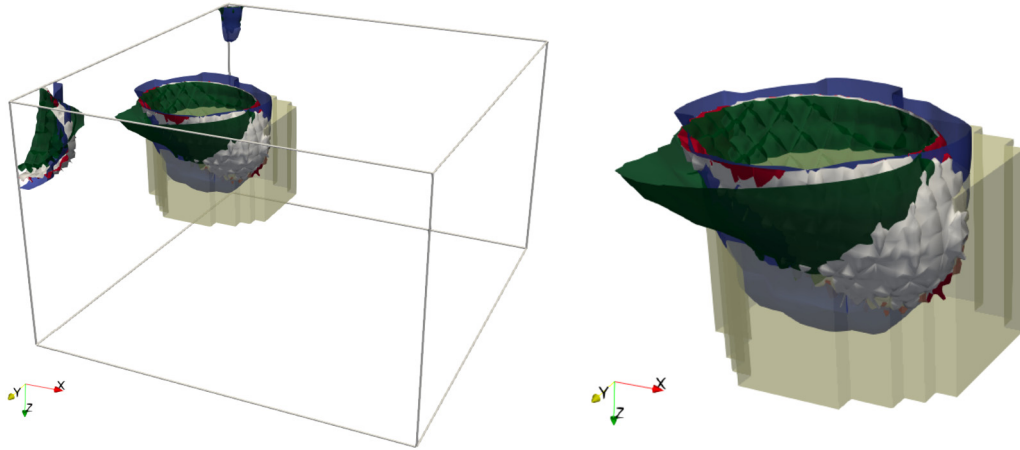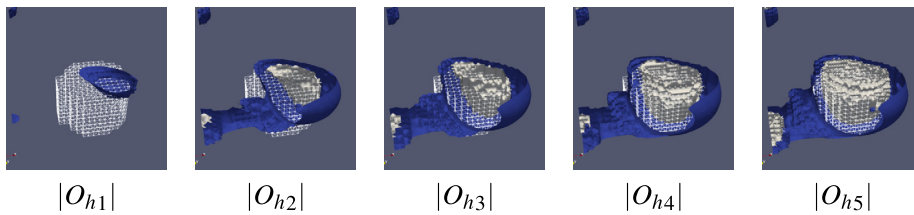
Fig. 3. Isosurfaces of reconstructions using different algorithms at $t = 2$ min. Table 2 presents the clarification for different colors of isosurfaces for the performed tests. (For interpretation of the colors in the figure(s), the reader is referred to the web version of this article.)

Table 2
Performance of different reconstruction algorithms for solution of the problem $\min_O J_\alpha(O) = \min_O \frac{1}{2}\|A(O) - d\|_2^2 + \frac{\alpha}{2}[O]^2$ for time $t = 2$ min. Here, different methods are: LS is the least squares method, AFEM2 is adaptive Algorithm 2 of Section 7, CG is conjugate gradient Algorithm 1 of Section 7, bal. is balancing principle.

Color in Fig. 3	Method	Reg. term	Reg. param.	Reg. method	Time (sec)
Blue	LS	$\|O\|_2^2$	$\alpha = 1$	-	9
White	AFEM2, $\beta = 0.5$	$\|\nabla O\|_2^2$	$\alpha = 1.46$	bal.	83
Red	LS	$\|\nabla O\|_2^2$	$\alpha = 1.31$	bal.	63
Green	CG	$\|O\|_2^2$	$\alpha = 0.1$	bal.	11
-	CG	$\|\nabla O\|_2^2$	$\alpha = 1$	-	6
-	CG	$\|O\|_2^2$	$\alpha = 1$	-	7

| $|O_{h1}|$ | $|O_{h2}|$ | $|O_{h3}|$ | $|O_{h4}|$ | $|O_{h5}|$ |

Fig. 4. Dynamics of reconstructed isosurfaces $|O_{hl}|$ on l times adaptively refined meshes at time $t = 2$ min using adaptive Algorithm 2 for solution of different problems: solution of problem (70) (blue isosurface) and solution of problem (71) (white isosurface). Both problems were computed with $\beta_{1,2} = 0.5$ in the refinement criterion. Exact scatterer is outlined by the finite element mesh. See Table 3 for computational time and Table 4 for convergence of this test at time $t = 2$ min and $\beta = 0.5$.

Test 1 (CG)

The goal of computations in this test was to check performance of the conjugate gradient Algorithm 1 (CG) and balancing principle for optimal choice of the regularization parameter α in the functional (23) for different regularization terms: namely, for regularization terms $\frac{\alpha}{2}\|O\|_2^2$ and $\frac{\alpha}{2}\|\nabla O\|_2^2$.

We start running the conjugate gradient Algorithm 1 with the initial guess $O_h^0 = 0$. The fixed point algorithm of [5] was used for optimal choice of the regularization parameter α which implemented balancing principle [34].

Convergence of the fixed point algorithm is presented in Fig. 1. As can be seen from the figure, for all test examples the optimal regularization parameter α was found on the interval $\alpha \in [0.4361, 0.4447]$ for the problem

$$\min_O J_\alpha(O) = \min_O \frac{1}{2}\|A(O) - d\|_2^2 + \frac{\alpha}{2}\|O\|^2 \tag{70}$$

and on the interval $[1.3392, 1.342]$ for the problem

$$\min_O J_\alpha(O) = \min_O \frac{1}{2}\|A(O) - d\|_2^2 + \frac{\alpha}{2}\|\nabla O\|^2. \tag{71}$$

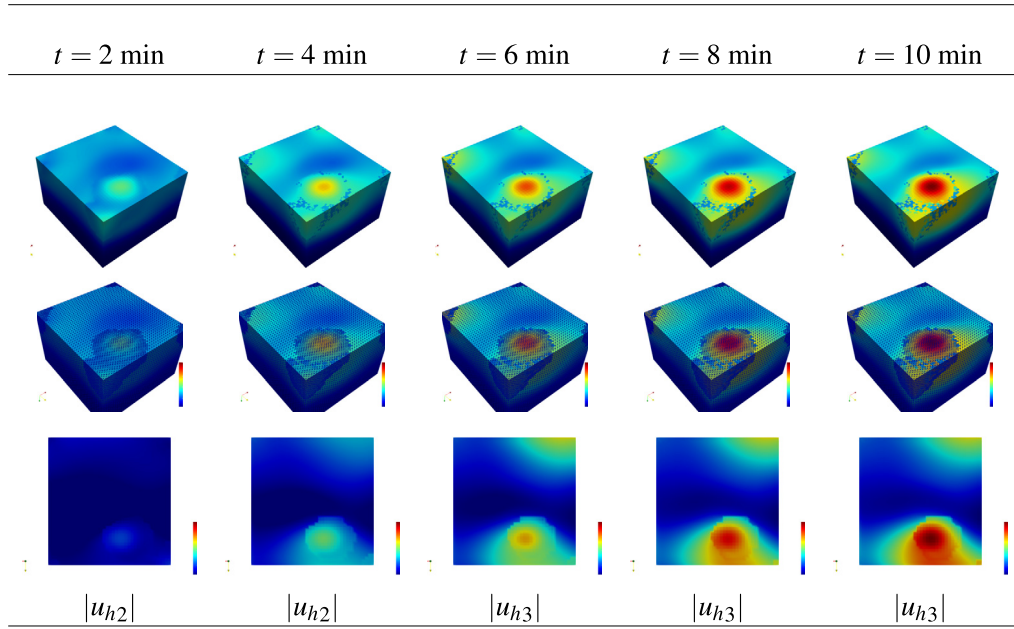| $t = 2$ min	$t = 4$ min	$t = 6$ min	$t = 8$ min	$t = 10$ min
$|u_{h2}|$	$|u_{h2}|$	$|u_{h3}|$	$|u_{h3}|$	$|u_{h3}|$

Fig. 5. Test 2: Reconstructions obtained by the adaptive algorithm of [5] with $\beta = 0.5$ in the refinement procedure. Top and middle lines: 3D surface solution $|u_{hl}|$, and $|u_{hl}|$ together with the refined mesh K_l, correspondingly. Bottom line: 2D slices of $|u_{hl}|$ passing through the point $(36, 21, 7)$. Here, l denotes the number of the locally refined mesh K_{hl} where the solution u_{hl} was obtained.
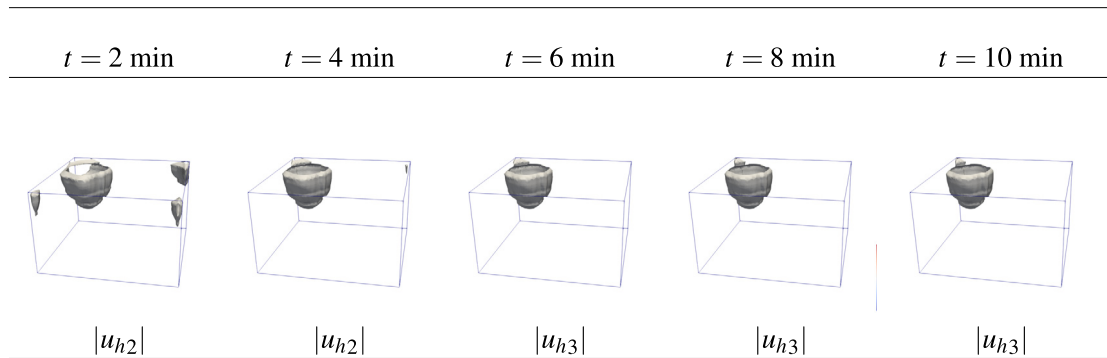

$t = 2$ min	$t = 4$ min	$t = 6$ min	$t = 8$ min	$t = 10$ min
$|u_{h2}|$	$|u_{h2}|$	$|u_{h3}|$	$|u_{h3}|$	$|u_{h3}|$

Fig. 6. Test 2: Reconstructions obtained by the adaptive algorithm of [5] with $\beta = 0.5$ in the refinement procedure. We present 3D slices of the reconstruction $|u_{hl}|$ at different times. Here, l denotes the number of the locally refined mesh $K_l := K_{hl}$ where the solution u_{hl} was obtained.

Table 2 shows performance of different reconstruction algorithms for solution of problems (70), (71) in terms of time. Using this table, we observe that all reconstruction algorithms with balancing principle usually requires more computational time than usual reconstruction algorithms with constant value of the regularization parameter α. Analyzing results of Fig. 1 and Table 2, we can conclude that the choice of the regularization parameter $\alpha = 1$ is a good one for solution of both problems (70) and (71). Thus, all further tests to check performance of Algorithms 2 (AFEM2) and 3 (AFEM3) we will perform for the solution of the problem (70) or (71) with the constant value of the regularization parameter $\alpha = 1$. See also Fig. 4.

Test 2 (AFEM1)

First we perform the three-dimensional AFEM computations using the adaptive algorithm of [5] which we will denote AFEM1 and briefly present below. Note that in [5] were performed only 2D AFEM computations. In AFEM1 algorithm, first the initial reconstruction O_0 has been obtained as minimization of the functional (23) with the operator $A : L_2 \to L_2$. Thus, the method of normal equations was used to get the solution

$$O_0 = (Ke^T Ke + \alpha I)^{-1} Ke^T d. \tag{72}$$

Here, Ke is the known kernel matrix resulted from discretization of the operator $A(O)$ in (21). Then the SVD-decomposition of $Ke = U \Sigma V^T$ was used in (72) to get the regularized least squares solution
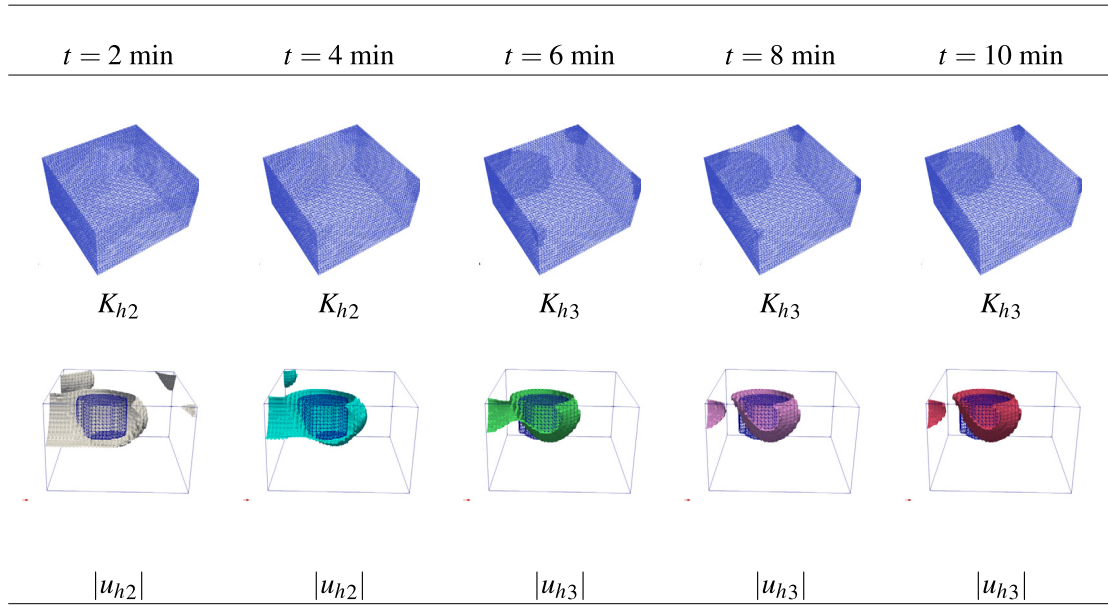
Fig. 7. Test 2: Reconstructions obtained by the adaptive algorithm of [5] with $\beta = 0.3$ in the refinement procedure. Top row: adaptively refined meshes for different times. Bottom line: 3D slices of the reconstruction $|u_{hl}|$ at different times. Here, l denotes the number of the locally refined mesh $K_l := K_{hl}$ where the solution u_{hl} was obtained.

$$O_0 = V(\Sigma^2 + \alpha I)^{-1}\Sigma U^T d. \tag{73}$$

Next, the adaptive finite element method was used for improvement of the already obtained least squares solution O_0 thorough the minimization of the following functional

$$J_\alpha(u) = \frac{1}{2}\|F(u) - O_0\|_2^2 + \frac{\alpha}{2}\|\nabla u\|_2^2, \tag{74}$$

where $F(u)$ is the convolution operator similar to that of [10]. Thus, the adaptive algorithm developed in [5] can be considered as an algorithm for image restoration where the actual values of the operator $A(O)$ were not used. We summarize it in the Algorithm 4.

Algorithm 4 Adaptive algorithm for image restoration (AFEM1).

1: First stage: generate the initial FEM mesh K_0 in Ω. Obtain the initial reconstruction O_0 on K_0 via (73).
2: Second stage: compute the sequence of reconstructions u_l, $l \geq 0$, on the refined meshes, in the following steps:
3: Use the fixed point algorithm (balancing principle) for determining the optimal regularization parameter α. Compute the finite element solution u_l on K_l using the finite element method for solution of the problem

$$\min_u J_\alpha(u) = \min_u \frac{1}{2}\|F(u) - O_0\|_2^2 + \frac{\alpha}{2}\|\nabla u\|_2^2. \tag{75}$$

4: Refine locally the mesh K_l at all points where

$$R(u_l) \geq \beta \max_\Omega R(u_l), \tag{76}$$

where $\beta \in (0, 1)$ and residual $R(u_l) := \|hu_l\|$ is computed on the mesh K_l.
5: Construct a new mesh K_{l+1} in Ω. Interpolate O_l to O_{l+1} and u_l to u_{l+1} using barycentric interpolation.
6: For the chosen tolerance θ, stop computing u_l at the iteration $M := l$ and obtain the function u_M if either $\|R(u_l)\|_{L_2(\Omega)} \leq \theta$ or norms $\|u_l\|_{L_2(\Omega)}$ are stabilized. Otherwise go to step 3.

The three-dimensional computations were performed with $\beta = 0.3, 0.5$ in the mesh refinement criterion (76). Such values of β allow locally refine the mesh exactly where the inclusion is located, see the middle line of Fig. 5 for $\beta = 0.5$ and the top line of Fig. 7 for $\beta = 0.3$.

The optimal value of the regularization parameter α in these computations was found on the interval $\alpha \in [0.47, 0.69]$ for all refined meshes. The optimal reconstructed solution $|u_h|$ was found on a two times refined mesh for times $t = 2$ min and $t = 4$ min and on a three-times locally refined mesh for times $t = 6, 8, 10$ min, see Fig. 5. The top and middle lines of Fig. 5 present 3D surface solution (with and without mesh). The bottom line of Fig. 5 shows two-dimensional slices of the computed solution $|u_{hl}|$ on l times adaptively refined mesh K_l passing through the point $(36, 21, 7)$. See also Fig. 6.
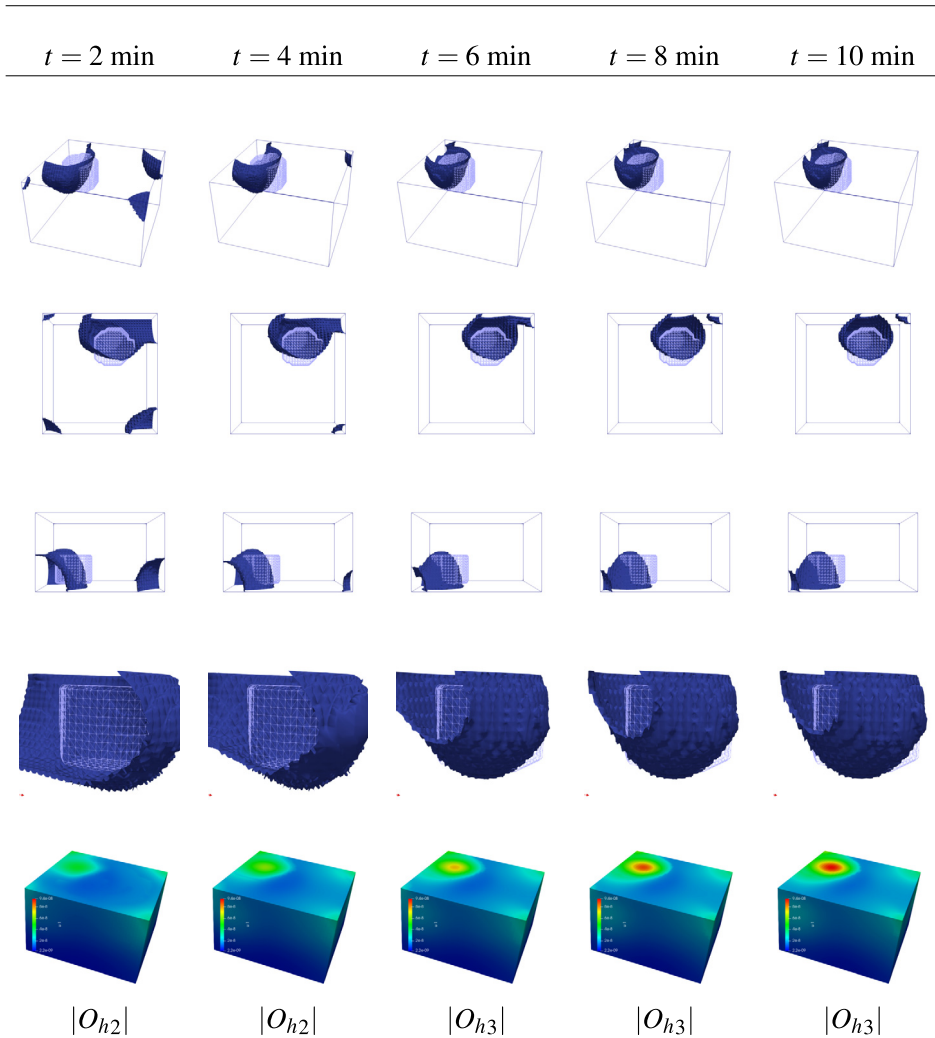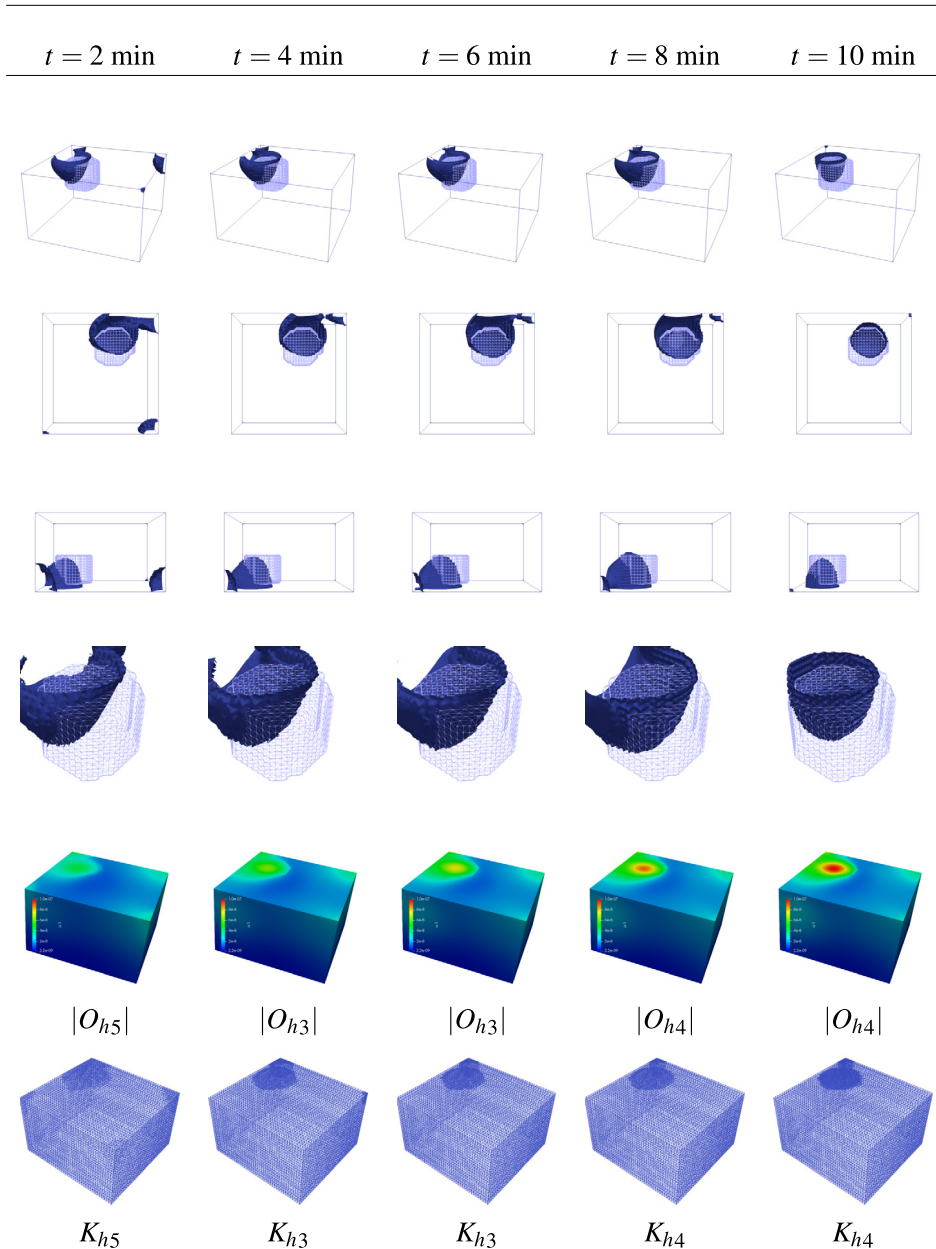
Fig. 8. Test 3: Reconstructions obtained by the adaptive Algorithm 2 with $\beta = \beta_1 = \beta_2 = 0.3$ in the refinement procedure of this algorithm. We show 3D slices of $|O_{hl}|$ obtained at different times on the l times locally refined mesh. Top row: prospect view, second row: xy-projection, third row: yz-projection. Fourth row: zoomed view of obtained $|O_{hl}|$. Bottom row: surface view of reconstructions. Exact scatterer on all figures is outlined by the finite element mesh.

Test 3 (AFEM2)

Now we test the performance of the adaptive Algorithm 2, AFEM2. Isosurfaces and surface plots of reconstructions are presented in Figs. 8 and 9, correspondingly, for $\beta_{1,2} = 0.3$ and $\beta_{1,2} = 0.5$ in the refinement criterion at step 3 of AFEM2.

Results in terms of computational time of AFEM2 for different parameters $\beta_{1,2}$ are presented in Table 3. Convergence tests for all times $t = 2, 4, 6, 8, 10$ are shown in Tables 4–8 for $\beta_{1,2} = 0.3, 0.5$, and $\beta_{1,2} = 0.7$ in the refinement criterion at step 3 of AFEM2. Using these tables we observe that the parameters $\beta_{1,2}$ control the number of the refined elements and thus, the number of the nodes in the refined mesh K_{hl}: the computational mesh K_{hl} is refined in very narrow region when $\beta_{1,2} = 0.7$, and when we choose $\beta_{1,2} = 0.3$ almost all elements in the finite element mesh K_{hl} are refined. Also, it is required more mesh refinements for $\beta_{1,2} = 0.7$ than for $\beta_{1,2} = 0.3, 0.5$ in order to achieve desired tolerance in the stopping criterion. Analyzing convergence results of Tables 4–8 we can conclude that parameter $\beta = 0.7$ provides not only narrow mesh refinement which don't cover the domain where the inclusion is located but also increasing in the computational gradient $\|g_l\|_2$. We observe that values $\beta_{1,2} = 0.3, 0.5$ are optimal one and provide decreasing of the computational gradient $\|g_l\|_2$ and refinement of the mesh K_{hl} exactly where the inclusion is located, see Figs. 8 and 9.

Analyzing results in Tables 4–8 and Figs. 8 and 9, we can conclude that the optimal reconstruction results in terms of time and convergence are obtained for $\beta = 0.3$ and $\beta = 0.5$. Using Figs. 8 and 9 we also observe that AFEM2 algorithm managed well reconstruct temperature changes in the object during the hyperthermia process.

Fig. 9. Test 3: Reconstructions obtained by the adaptive Algorithm 2 with $\beta = \beta_1 = \beta_2 = 0.5$ in the refinement procedure of this algorithm. We show 3D slices of $|O_{hl}|$ obtained at different times on the l times locally refined mesh. Top row: prospect view, second row: xy-projection, third row: yz-projection. Fourth row: zoomed view of obtained $|O_{hl}|$ superimposed with exact scatterer. Fifth row: surface view of reconstruction. Bottom row: adaptively refined meshes K_{hl} corresponding to the obtained reconstructions $|O_{hl}|$. Exact scatterer in the first - fourth rows is outlined by the finite element mesh.

Test 4 (AFEM3)

Isosurfaces of reconstructions using adaptive Algorithm 3 are the same as for the adaptive Algorithm 2, see Figs. 8 and 9 and Tables 4–8, and we are not presenting them here.

Results in terms of computational time of the adaptive Algorithm 3 for different parameters $\beta_{1,2}$ are also similar to the results obtained in adaptive Algorithm 2. Thus, both algorithms have the same performance.

9. Concluding remarks

An adaptive finite element method for the numerical solution of an electromagnetic volume integral equation was presented and applied to the real experimental scenario.

Table 3

Test 3: Performance of AFEM2 in terms of computational time in seconds and relative time for solution of the problem (71) with $\alpha = 1$ and different parameters $\beta := \beta_{1,2}$. Here, $K_l := K_{hl}$ represents the finite element mesh refined l times where the final reconstruction O_{hl} was obtained. See Tables 4–8 for number of nodes and convergence on the refined meshes K_l.

β	$K_l := K_{hl}$	Time (sec)	Relative time
		$t = 2$ min	
0.3	K_2	17	7.1138ee-05
0.5	K_5	26	1.6405e-05
0.7	K_6	21	1.0651e-05
		$t = 4$ min	
0.3	K_2	17	7.2430e-05
0.5	K_3	16	3.3410e-05
0.7	K_5	26	1.2177e-05
		$t = 6$ min	
0.3	K_3	24	4.0676e-05
0.5	K_3	16	3.3848e-05
0.7	K_6	26	1.2323e-05
		$t = 8$ min	
0.3	K_3	24	4.1655e-05
0.5	K_4	21	2.2746e-05
0.7	K_6	25	1.1938e-05
		$t = 10$ min	
0.3	K_3	23	4.0213e-05
0.5	K_4	31	1.7863e-05
0.7	K_6	25	1.1956e-05

Table 4

Test 3: Convergence of the adaptive Algorithm 3 (AFEM3) on a locally refined meshes $K_l := K_{hl}$ for different $\beta := \beta_{1,2}$ at the time $t = 2$ min. Here, l is the number of the refinements of the mesh K_l, nno is the number of nodes in the mesh K_l.

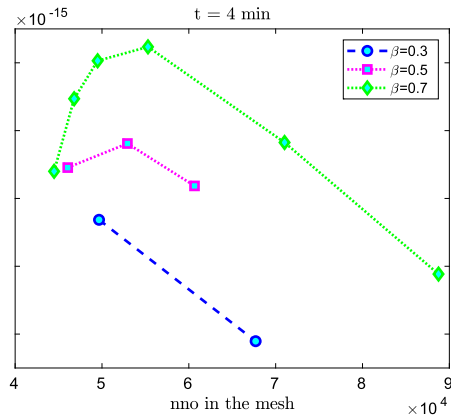| β	l	nno	$\|g_l\|_2$
		$t = 2$ min	
0.3	1	50161	$0.1056 \cdot 10^{-14}$
	2	69325	$0.0819 \cdot 10^{-14}$
0.5	1	45309	$0.1173 \cdot 10^{-14}$
	2	49959	$0.1279 \cdot 10^{-14}$
	3	55526	$0.1259 \cdot 10^{-14}$
	4	67176	$0.1133 \cdot 10^{-14}$
	5	99010	$0.078 \cdot 10^{-14}$
0.7	1	44254	$0.1158 \cdot 10^{-14}$
	2	45868	$0.1301 \cdot 10^{-14}$
	3	47874	$0.1396 \cdot 10^{-14}$
	4	52057	$0.1487 \cdot 10^{-14}$
	5	62955	$0.1448 \cdot 10^{-14}$
	6	75613	$0.1255 \cdot 10^{-14}$
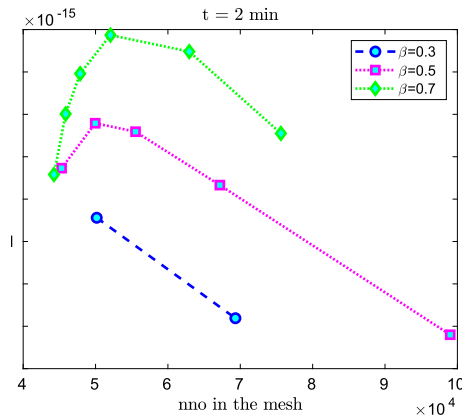
The problem was formulated as an optimal control problem for minimization of Tikhonov's regularization functional. A posteriori error estimates in the obtained finite element reconstruction and error in Tikhonov's functional were derived. Based on these estimates, adaptive finite element algorithms were formulated and tested on 3D reconstructions of a target during the process of microwave thermometry. Our numerical results show that AFEM-based algorithms are a reliable and efficient tool for solution of microwave thermometry problem in real time. Our numerical tests also show that an adaptive finite element method improves the reconstruction obtained by the least squares method via local adaptive mesh refinements.

Future work can be related to the testing of the developed algorithms on large computational meshes using MPI in real time. The computational time for a large number of meshes processed in a single-core processor can be estimated by applying the results of Table 3. For example, using formula (69) and Table 3, we can estimate computational time of both algorithms, AFEM2 or AFEM3, on the coarse mesh consisting of $2 \cdot 10^6$ nodes without any adaptive refinement: the computational time will be computed for $l = 0$ as $t = Tr \cdot nno \approx Const. \cdot 10^{-5} \cdot 2 \cdot 10^6 \approx Const. \cdot 20$, $Const. \in [1.0651, 7.243]$ seconds which is appropriate for real-time monitoring in different microwave applications.

Table 5

Test 3: Convergence of the adaptive Algorithm 3 (AFEM3) on a locally refined meshes $K_l := K_{hl}$ for different $\beta := \beta_{1,2}$ at the time $t = 4$ min. Here, l is the number of the refinements of the mesh K_l, nno is number of nodes in the mesh K_l.

β	l	nno	$\|g_l\|_2$
		$t = 4$ min	
0.3	1	49660	$0.1737 \cdot 10^{-14}$
	2	67694	$0.1379 \cdot 10^{-14}$
0.5	1	46054	$0.1891 \cdot 10^{-14}$
	2	52927	$0.1962 \cdot 10^{-14}$
	3	60654	$0.1837 \cdot 10^{-14}$
0.7	1	44486	$0.1880 \cdot 10^{-14}$
	2	46795	$0.2094 \cdot 10^{-14}$
	3	49499	$0.2206 \cdot 10^{-14}$
	4	55297	$0.2247 \cdot 10^{-14}$
	5	71024	$0.1965 \cdot 10^{-14}$
	6	88752	$0.1577 \cdot 10^{-14}$

Table 6

Test 3: Convergence of the adaptive Algorithm 3 (AFEM3) on a locally refined meshes $K_l := K_{hl}$ for different $\beta := \beta_{1,2}$ at the time $t = 6$ min. Here, l is the number of the refinements of the mesh K_l, nno is number of nodes in the mesh K_l.
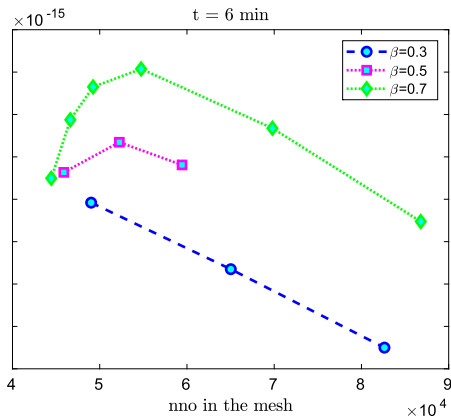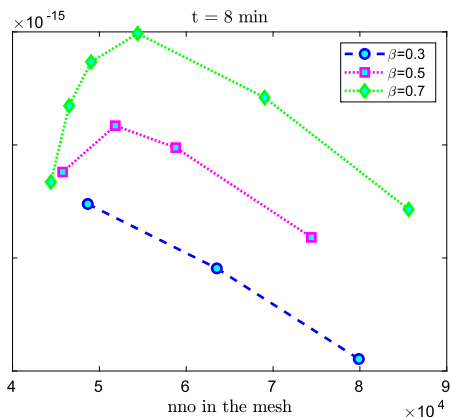
β	l	nno	$\|g_l\|_2$
		$t = 6$ min	
0.3	1	49017	$0.1984 \cdot 10^{-14}$
	2	65024	$0.1670 \cdot 10^{-14}$
	3	82634	$0.1300 \cdot 10^{-14}$
0.5	1	45881	$0.2127 \cdot 10^{-14}$
	2	52250	$0.2269 \cdot 10^{-14}$
	3	59435	$0.2162 \cdot 10^{-14}$
0.7	1	44444	$0.2099 \cdot 10^{-14}$
	2	46629	$0.2375 \cdot 10^{-14}$
	3	49238	$0.2530 \cdot 10^{-14}$
	4	54744	$0.2615 \cdot 10^{-14}$
	5	69797	$0.2335 \cdot 10^{-14}$
	6	86801	$0.1895 \cdot 10^{-14}$

Table 7

Test 3: Convergence of the adaptive Algorithm 3 (AFEM3) on a locally refined meshes $K_l := K_{hl}$ for different $\beta := \beta_{1,2}$ at the time $t = 8$ min. Here, l is the number of the refinements of the mesh K_l, nno is number of nodes in the mesh K_l.

β	l	nno	$\|g_l\|_2$
		$t = 8$ min	
0.3	1	48660	$0.2239 \cdot 10^{-14}$
	2	63520	$0.1954 \cdot 10^{-14}$
	3	79876	$0.1553 \cdot 10^{-14}$
0.5	1	45769	$0.2380 \cdot 10^{-14}$
	2	51835	$0.2585 \cdot 10^{-14}$
	3	58793	$0.2488 \cdot 10^{-14}$
	4	74408	$0.2091 \cdot 10^{-14}$
0.7	1	44412	$0.2336 \cdot 10^{-14}$
	2	46515	$0.2673 \cdot 10^{-14}$
	3	49049	$0.2867 \cdot 10^{-14}$
	4	54411	$0.2993 \cdot 10^{-14}$
	5	69029	$0.2710 \cdot 10^{-14}$
	6	85608	$0.2215 \cdot 10^{-14}$

Table 8

Test 3: Convergence of the adaptive Algorithm 3 (AFEM3) on a locally refined meshes $K_l := K_{hl}$ for different $\beta := \beta_{1,2}$ at the time $t = 10$ min. Here, l is the number of the refinements of the mesh K_l, nno is number of nodes in the mesh K_l.

β	l	nno	$\|g_l\|_2$
		$t = 10$ min	
0.3	1	48544	$0.2381 \cdot 10^{-14}$
	2	63059	$0.2104 \cdot 10^{-14}$
	3	79050	$0.1685 \cdot 10^{-14}$
0.5	1	45739	$0.2523 \cdot 10^{-14}$
	2	51733	$0.2760 \cdot 10^{-14}$
	3	58610	$0.2665 \cdot 10^{-14}$
	4	73954	$0.2255 \cdot 10^{-14}$
	5	117054	$0.1371 \cdot 10^{-14}$
0.7	1	44415	$0.2473 \cdot 10^{-14}$
	2	46519	$0.2844 \cdot 10^{-14}$
	3	49050	$0.3058 \cdot 10^{-14}$
	4	54408	$0.3201 \cdot 10^{-14}$
	5	68876	$0.2911 \cdot 10^{-14}$
	6	85235	$0.2389 \cdot 10^{-14}$
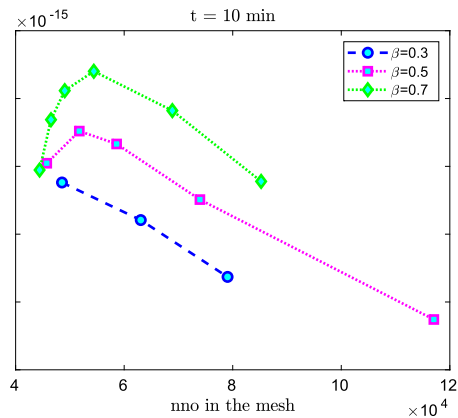
We hope that the method presented in the paper can be adopted in different microwave applications to obtain real-time reconstructed images.

Declaration of competing interest

The authors declare that they have no known competing financial interests or personal relationships that could have appeared to influence the work reported in this paper.

Acknowledgement

References

[1] M. Asadzadeh, K. Eriksson, On adaptive finite element methods for Fredholm integral equations of the second kind, SIAM J. Numer. Anal. 31 (3) (1994) 831–855.

[2] W.C. Chew, Waves and Fields in Inhomogeneous Media, IEEE Press, New York, 1995.

[3] M. Haynes, J. Stang, M. Moghaddam, Real-time microwave imaging of differential temperature for thermal therapy monitoring, IEEE Trans. Biomed. Eng. 61 (6) (June 2014) 1787–1797.

[4] M. Haynes, M. Moghaddam, Vector Green's function for S-parameter measurements of the electromagnetic volume integral equation, IEEE Trans. Antennas Propag. 60 (3) (2012) 1400–1413, https://doi.org/10.1109/tap.2011.2180324.

[5] M.G. Aram, L. Beilina, H. Dobsicek Trefna, Microwave thermometry with potential application in non-invasive monitoring of hyperthermia, J. Inverse Ill-Posed Probl. (2020), https://doi.org/10.1515/jiip-2020-0102.

[6] P.B. Monk, Finite Element Methods for Maxwell's Equations, Oxford University Press, 2003.

[7] R. Kress, Linear Integral Equations, Springer-Verlag, Berlin, 1989.

[8] C.W. Groetsch, Inverse Problems in the Mathematical Sciences, Friedr. Vieweg & Sohn Verlagsgesellschaft, Braunschweig/Wiesbaden, Germany, 1993.

[9] A.N. Tikhonov, A.V. Goncharsky, V.V. Stepanov, A.G. Yagola, Numerical Methods for the Solution of Ill-Posed Problems, Kluwer, London, 1995.

[10] N. Koshev, L. Beilina, An adaptive finite element method for Fredholm integral equations of the first kind and its verification on experimental data, Cent. Eur. J. Math. 11 (8) (2013) 1489–1509, https://doi.org/10.2478/s11533-013-0247-3.

[11] R. Hoppe, T.L. Phillips, M. Roach III, Hyperthermia, in: Textbook of Radiation Oncology: Expert Consult, 3rd ed., Elsevier, Amsterdam, the Netherlands, 2010, pp. 1564–1593, ch. 74.

[12] Nikola Cihoric, Alexandros Tsikkinis, Gerard van Rhoon, Hans Crezee, Daniel M. Aebersold, Stephan Bodis, Marcus Beck, Jacek Nadobny, Volker Budach, Peter Wust, Pirus Ghadjar, Hyperthermia-related clinical trials on cancer treatment within the ClinicalTrials.gov registry, Int. J. Hyperth. 31 (6) (2015) 609–614, https://doi.org/10.3109/02656736.2015.1040471.

[13] N.R. Datta, S.G. Ordóñez, U.S. Gaipl, et al., Local hyperthermia combined with radiotherapy and-/or chemotherapy: recent advances and promises for the future, Cancer Treat. Rev. 41 (9) (2015) 742–753, https://doi.org/10.1016/j.ctrv.2015.05.009.

[14] J.C. Bolomey, L. Jofre, G. Peronnet, On the possible use of microwave-active imaging for remote thermal sensing, IEEE Trans. Microw. Theory Tech. 31 (9) (Sep. 1983) 777–781.

[15] M. Haynes, J. Stang, M. Moghaddam, Real-time microwave imaging of differential temperature for thermal therapy monitoring, IEEE Trans. Biomed. Eng. 61 (6) (June 2014) 1787–1797.

[16] G. Chen, M. Moghaddam, J. Stang, M. Haynes, Real-time 3D microwave monitoring of thermal therapy, Patent Application Publication, Pub. No.US2020/0093374 A1 Mar. 2020.

[17] M. Lazebnik, M.C. Converse, J.H. Booske, S.C. Hagness, Ultrawideband temperature-dependent dielectric properties of animal liver tissue in the microwave frequency range, Phys. Med. Biol. 51 (2006) 1941–1955.

[18] D. Colton, R. Kress, Time harmonic electromagnetic waves in an inhomogeneous medium, Proc. R. Soc. Edinb., Sect. A, Math. 116 (3–4) (1990) 279–293.

[19] A.B. Samokhin, Y.G. Smirnov, Uniqueness and existence theorems for solving problems of scattering electromagnetic waves by anisotropic bodies, Dokl. Math. 103 (1) (2021) 50–53.

[20] A. Taflove, S. Hagness, Computational electrodynamics: the finite difference time domain method, 2005.

[21] Ivan G. Graham, Thomas Y. Hou, Omar Lakkis, Robert Scheichl (Eds.), Numerical Analysis of Multiscale Problems, Lecture Notes in Computational Science and Engineering, vol. 83, Springer, Heidelberg, 2012.

[22] Otmar Scherzer, Markus Grasmair, Harald Grossauer, Markus Haltmeier, Frank Lenzen, Handbook of Mathematical Methods in Imaging, 2nd ed., Springer, 2015.

[23] L. Beilina, Yu.G. Smirnov (Eds.), Nonlinear and Inverse Problems in Electromagnetics, Springer Proceedings in Mathematics and Statistics, 2017.

[24] L. Beilina, Yu.V. Shestopalov (Eds.), Inverse Problems and Large-Scale Computations, Springer Proceedings in Mathematics and Statistics, vol. 52, 2013.

[25] E.M. Karchevskii, L. Beilina, A.O. Spiridonov, A.I. Repina, Reconstruction of dielectric constants of multi-layered optical fibers using propagation constants measurements, Appl. Comput. Math. 15 (3) (2016) 346–358.

[26] L. Beilina, G. Guillot, K. Niinimäki, The finite element method and balancing principle for magnetic resonance imaging, in: Mathematical and Numerical Approaches for Multi-Wave Inverse Problems, CIRM 2019, in: Springer Proceedings in Mathematics & Statistics, vol. 328, Springer, Cham, 2020, pp. 127–142.

[27] S.C. Brenner, L.R. Scott, The Mathematical Theory of Finite Element Methods, 2nd edn., Springer-Verlag, New York, 2002.

[28] M. Křížek, P. Neittaanmäki, Finite Element Approximation of Variational Problems and Applications, Longman, Harlow, 1990.

[29] L. Beilina, M.V. Klibanov, Approximate Global Convergence and Adaptivity for Coefficient Inverse Problems, Springer, New-York, 2012.

[30] K. Eriksson, D. Estep, C. Johnson, Calculus in Several Dimensions, Springer, Berlin, 2004.

[31] C. Johnson, A. Szepessy, Adaptive finite element methods for conservation laws based on a posteriori error estimation, Commun. Pure Appl. Math. 48 (1995) 199–234.

[32] L.R. Scott, S. Zhang, Finite element interpolation of nonsmooth functions satisfying boundary conditions, Math. Comput. 54 (1990) 483–493.

[33] H. Ammari, An Introduction to Mathematics of Emerging Biomedical Imaging, Springer, 2008.

[34] K. Ito, B. Jin, Inverse Problems: Tikhonov Theory and Algorithms, Series on Applied Mathematics, vol. 22, World Scientific, 2015.

[35] CST Studio Suite, CST microwave studio, http://www.cst.com, 2019.

[36] PETSC, the software package, https://petsc.org/.

[37] WavES, the software package, http://www.waves24.com.

[38] WavES code for implementation of AFEM algorithms for VIE, https://github.com/ProjectWaves24/.